Geomechanics for Energy and the Environment 34 (2023) 100472

Contents lists available at ScienceDirect

Geomechanics for Energy and the Environment

journal homepage: www.elsevier.com/locate/gete

Thermo-hydro-mechanical analysis of the complete lifetime of the bentonite barrier in the FEBEX in-situ test

Jose A. Bosch [a,*], Yafei Qiao [b,c], Alessio Ferrari [a,d], Lyesse Laloui [a]

[a] École Polytechnique Fédérale de Lausanne, EPFL, Station 18, CH-1015 Lausanne, Switzerland
[b] Department of Geotechnical Engineering, College of Civil Engineering, Tongji University, Shanghai, China
[c] Key Laboratory of Geotechnical and Underground Engineering of the Ministry of Education, Tongji University, Shanghai, China
[d] Università degli Studi di Palermo, Palermo, Italy

ARTICLE INFO

Article history:
Received 21 May 2021
Received in revised form 24 April 2023
Accepted 27 April 2023
Available online 3 May 2023

Editors-in-Chief:
Professor Lyesse Laloui and Professor Tomasz Hueckel

Keywords:
Nuclear waste disposal
Bentonite barriers
Elastoplasticity
Thermo-hydro-mechanical coupling
Unsaturated soils

ABSTRACT

The FEBEX test was a large-scale demonstration project for the deep geological disposal concept of nuclear waste involving bentonite seals that lasted 18 years. One of the objectives of the test was to evaluate the capabilities of numerical methods to provide reliable predictions of the physical processes in a geological repository. Although previous studies have demonstrated the performance of current models of water, vapour and heat flow to capture the evolution of temperature and relative humidity, some uncertainties remain in the capabilities of constitutive models to predict and interpret the stress–strain behaviour of the bentonite. In this paper a recently developed thermo-hydro-mechanical (THM) elastoplastic constitutive model is used to analyse the bentonite barrier of the FEBEX test by means of the Finite Element method. The model features a two-way hydro-mechanical coupling and includes thermo-plasticity. The associated water retention formulation distinguishes the behaviour of adsorbed water and free water. The predictive capabilities of the model are tested by calibrating the material parameters on the sole basis of laboratory tests. Good predictions of total stress, dry density and water content are obtained and the analysis of the computed THM stress paths provides new insights on the causes of the final heterogeneous state of the bentonite barrier.

1. Introduction

The Full-scale Engineered Barriers Experiment (FEBEX) was an 18 years-long experiment carried out in the Grimsel underground laboratory, in Switzerland, in order to demonstrate the feasibility of a geological disposal concept for high-level radioactive waste (HLW).[1] It adopted the Spanish reference concept for geological disposal of HLWs, involving a clay buffer constructed with highly compacted blocks of bentonite, constituting the so-called engineered barrier system (EBS). One of the main objectives of that experiment was to aid the development and evaluation of Thermo-Hydro-Mechanical (THM) numerical codes for predicting the long term evolution of nuclear waste repositories. In this context the test was extensively monitored. Among other variables, temperature, water pressure, relative humidity and total pressure were measured during the test at several locations in the bentonite, providing 18 years of monitored data.

The layout of the FEBEX test is shown in Fig. 1. A tunnel of 2.28 m in diameter was excavated in the central Aare granitic formation. Two heaters, with dimensions and weight representative of real canisters, were emplaced inside a steel liner fixed along the axis of the tunnel, surrounded by highly compacted bentonite blocks at unsaturated state, sealed by a concrete plug. The heating sequence started in 1997 and after 5 years of continued heating, the first heater was switched off and the partial dismantling of the test took place (Fig. 1b). The second heater was not switched off until 2015 after which the second and final dismantling of the test took place. The symmetrical design and two dismantling stages provided the opportunity to measure the water content and dry density distribution of the bentonite barrier at two different times.

Many studies have been devoted to the numerical simulation, prediction and interpretation of the FEBEX test performance. In many cases, simple stress–strain relationships for bentonite have been considered. Gens et al.[2] performed a preliminary analysis of the THM response of the test, featuring a one-dimensional analysis of a section representative of the contact with a heater. Using a coupled THM formulation, the analysis highlighted the influence of a number of phenomena, such as vapour diffusion due to the large thermal gradients. The mechanical behaviour of bentonite was modelled using a state surface approach. A benchmark study comparing the results of predictive analysis for the first five years of operation, involving several modelling groups was presented in Ref. 3. The comparison highlighted the

* Corresponding author.
E-mail address: jose.boschllufriu@epfl.ch (J.A. Bosch).

https://doi.org/10.1016/j.gete.2023.100472

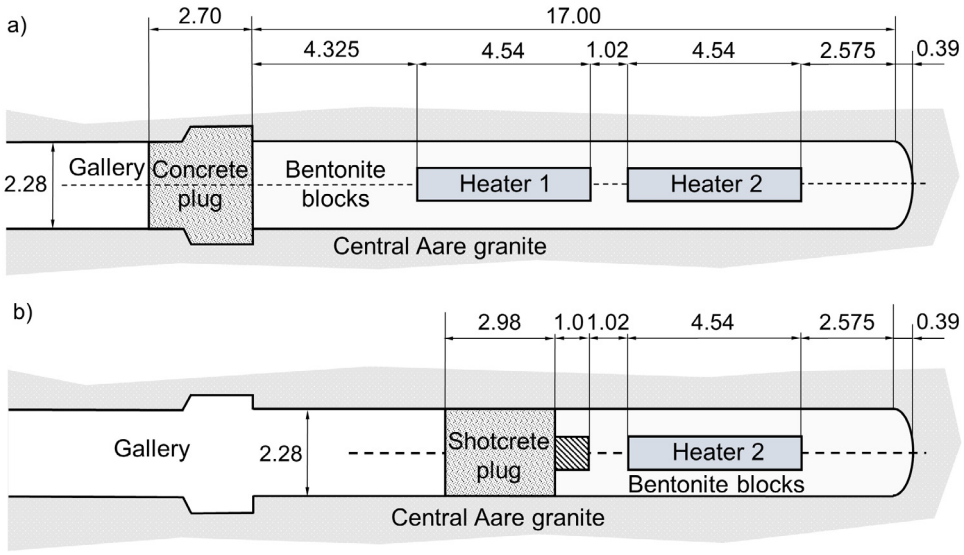

Fig. 1. Layout of the FEBEX experiment (a) during the first 5 years of operation, between 1997 and 2002, and (b) after the first dismantling until 2015.

need to consider coupled THM formulations in order to obtain a consistent reproduction of the evolution of all variables. As measurements after the dismantling were not available, all models in that benchmark used elastic stress–strain relationships for the bentonite behaviour.

However, the behaviour of bentonite may require more advanced constitutive models. As a matter of fact, Lloret et al.[4] demonstrated a clear stress path-dependent behaviour of the FEBEX bentonite when it is subjected to hydro-mechanical loads representative of those in a deep repository. While some modelling benchmarks of the in situ test have been reported recently (e.g. Ref. 5), few analyses in the literature report the ability of mechanical constitutive models to reproduce both laboratory and full-scale emplacement tests, and therefore their full predictive capabilities are difficult to assess. Gens et al.[6] presented a comprehensive analysis of the test performance of the first 5 years of heating, using the THM formulation presented by Olivella et al.[7] and a modified BBM elasto-plastic model for the bentonite.[3] The mechanical parameters for the analysis were calibrated with a swelling pressure test. A good replication of the test performance in terms of the data monitored during the test was obtained and the state of the barrier after the first dismantling of the test was well predicted. With the same model, Sánchez et al.[8,9] analysed the first and second dismantling of the test, including the cooling effects and the unloading of the bentonite barrier upon retrieval of the heaters. While globally the predictions were satisfactory, some discrepancies were found in the final saturation state.[9]

Dupray et al.[10] performed a numerical analysis of the FEBEX test up to the first dismantling stage focusing on the interpretation of bentonite based on a thermo-plasticity approach using the ACMEG-TS model.[11] Thus, additional plastic mechanisms were considered, highlighting how the coupling between swelling pressure and water retention can influence the results, specifically regarding the swelling-collapse of bentonite upon hydration and drying. The influence of water retention behaviour was also highlighted by Ref. 9, who reported a significant impact on the predicted saturation front. However, the coupling of water retention with deformation was left outside the scope of that study. In fact, in spite of many advances in the constitutive modelling of bentonite behaviour at the laboratory scale (e.g. Refs. 12–15), including new water retention models (e.g. Refs. 16, 17) their use for the assessment of bentonite barriers is not common.

This paper aims to fill this gap presenting a THM analysis of the bentonite barrier during the 18 years of operation of the FEBEX in situ test, with the recent hydro-mechanical model presented in Refs. 18, 19 extended to thermo-plasticity. One of the novelties of the analysis concerns the two-way coupling between mechanics and water retention, which takes explicitly into account a distinction between adsorbed water and free water. The main objectives are to provide an interpretation of the in situ test that includes hydro-mechanical couplings, and to validate the predictive capabilities of the constitutive model from laboratory tests to the repository scale. First the mathematical THM formulation used is described. Then, the finite element model used to simulate the FEBEX test is presented, including the determination of the material parameters. Since the focus of the study was the assessment of the predictive capabilities of the stress–strain constitutive model, the material parameters of the bentonite were calibrated on the sole basis of laboratory data. The modelling results of the THM bentonite response are then analysed, with a focus on the water content and dry density distribution. Finally, a link is made between the behaviour of bentonite measured at the elementary scale and the behaviour modelled at field scale, revealing how the local response of bentonite influences the global distribution of dry density.

2. THM formulation

2.1. Balance and field equations

The THM coupled formulation used in this work has been widely reported and validated[20–22] and it is implemented in the computer code LAGAMINE.[23] For the sake of conciseness only a summary is given in the following. The theory of mixtures following the compositional approach is used to formulate the THM processes in geological media.[24] The balance equations are established in terms of species (i.e. solid, water and dry air) and four primary state variables are used to describe the state of the material: gas pressure p_g, water pressure p_w, temperature T, and the displacement vector $\mathbf{u}$. Large deformations are considered using an updated Lagrangian formulation.[21] All fluid and thermal fluxes are expressed with respect to the solid skeleton. The effects of skeleton deformation on fluxes are taken into account at the nodal level.[20]

Changes in porosity in a volume of mixture V, are computed from the mass balance of solids in the current configuration:

$$\frac{\partial}{\partial t}\left[\rho_s\left(1-n\right)V\right]=0 \tag{1}$$

Where t is time, ρ refers to density and the subscript s to the solid species. The mass conservation equations for the water (subscript w) and gas (subscript g) species are, respectively:

$$\frac{\partial}{\partial t}\left(\rho_w n S_r\right) + \operatorname{div}\left(\rho_w \mathbf{f}_w\right) - Q_w + \frac{\partial}{\partial t}\left[\rho_v n\left(1-S_r\right)\right] + \operatorname{div}\left(\mathbf{i}_v + \rho_v \mathbf{f}_g\right) - Q_v = 0 \tag{2}$$

$$\frac{\partial}{\partial t}\left[\rho_a n\left(1-S_r\right)\right] + \operatorname{div}\left(\mathbf{i}_a + \rho_a \mathbf{f}_g\right) - Q_a + \frac{\partial}{\partial t}\left(H\rho_a n S_r\right) + \operatorname{div}\left(H\rho_a \mathbf{f}_w\right) - Q_{da} = 0 \tag{3}$$

where the subscript v stands for vapour phase, the subscript a for dry air and the subscript da for dissolved air in the liquid phase, $\mathbf{f}$ indicates advective fluxes, $\mathbf{i}$ diffusive fluxes, Q stands for the external sources, S_r is the degree of water saturation, and H refers to the Henry constant which indicates the proportion of dissolved air in the liquid. Assuming that the temperature is in equilibrium across the different components, the energy balance equation reads:

$$\frac{\partial S_T}{\partial t} + L\frac{\partial}{\partial t}\left[\rho_v n\left(1-S_r\right)\right] + \operatorname{div}\left(\mathbf{f}_T\right) + L\frac{\partial}{\partial t}\left(\mathbf{i}_v + \rho_v \mathbf{f}_g\right) - Q_T = 0 \tag{4}$$

where L is the latent heat of water vaporisation (considered constant as $2.5 \cdot 10^6$ J/kg), $\mathbf{f}_T$ is the thermal flux, Q_T refers to the heat source and S_T is the enthalpy of the medium, given by:

$$S_T = \left[\left(1-n\right)\rho_s c_{p,s} + n S_r \rho_w c_{p,w} + n\left(1-S_r\right) \times \left(\rho_a c_{p,a} + \rho_v c_{p,v}\right)\right]\left(T - T_0\right) \tag{5}$$

where $c_{p,i}$ corresponds to the heat capacity of the species i, T is the current temperature and T_0 is a reference temperature. The equilibrium of the medium is established as:

$$\operatorname{div}\left(\boldsymbol{\sigma}\right) + \mathbf{b} = \mathbf{0} \tag{6}$$

where $\mathbf{b}$ is the body force vector.

2.2. Thermal and hydraulic constitutive laws

The bulk density of liquid water is assumed to depend on p_w and T according to:

$$\rho_w = \rho_{w0}\left[1 + \chi_w\left(p_w - p_{w0}\right) - \beta_w\left(T - T_r\right)\right] \tag{7}$$

Where p_w is water pressure, ρ_{w0} is the bulk water reference density at T_r and at reference pressure p_{w0}, χ_w is the water compressibility and β_w is the water thermal expansion coefficient. The dynamic viscosity of bulk water μ_w evolves with T according to the empirical equation[25]:

$$\mu_w = 0.6612\left(T - 229\right)^{-1.56} \tag{8}$$

where μ_w is expressed in Pa· s and T in Kelvin degrees.

The advective water flux is modelled by means of Darcy's law assuming an isotropic permeability tensor:

$$\mathbf{f}_w = -\frac{\mathbf{I} k_f k_{rw}}{\mu_w}\left[\operatorname{grad}\left(p_w + \rho_w g z\right)\right] \tag{9}$$

where, k_f is the intrinsic permeability, k_{rw} is the relative permeability, g is the acceleration of gravity and $\mathbf{I}$ is the identity matrix. The relative permeability evolves with the degree of saturation, S_r following an exponential law:

$$k_{rw} = S_r^{\alpha_k} \tag{10}$$

where α_k is a material parameter. The influence of deformation on the intrinsic permeability is taken into account by means of a modified Kozeny–Carman formula[22]:

$$k_f = k_{f,0}\frac{\left(1-n_0\right)^{MKC}}{n_0^{NKC}}\frac{n^{NKC}}{\left(1-n\right)^{MKC}} \tag{11}$$

where $k_{f,0}$ is the initial intrinsic permeability for a porosity n_0, n stands for the current porosity and MKC and NKC are material parameters.

The vapour density is computed as:

$$\rho_v = \exp\left[-\frac{sM_w}{RT\rho_w}\right]p_{v0}\frac{M_w}{RT} \tag{12}$$

where M_w is the molar mass of water, R = 8.314 J/mol K, is the gas constant, s is the suction, and p_{v0} is the saturated vapour pressure. The latter is computed as $p_{v0} = 112.659\exp(-5192.74°\mathrm{K}/T)$ MPa.[22] The air density is computed considering that the gas phase as an ideal gas and that Dalton's law applies:

$$\rho_a = \frac{p_a M_a}{RT} = \frac{\left(p_g - p_v\right)M_a}{RT} = \left(\frac{p_g M_a}{RT} - \frac{\rho_v}{M_w}\right)M_a \tag{13}$$

where p_a is the air pressure, p_g is the gas pressure and $M_a = 28.8 \cdot 10^{-3}$ kg/mol is the molar mass of dry air.

Vapour is assumed to flow according to Fick's law in porous medium:

$$\mathbf{i}_v = -\mathbf{i}_a = n\left(1-S_r\right)\tau D\rho_g \operatorname{grad}\left(\rho_v\right) \tag{14}$$

where $D = 5.893\cdot 10^{-6}(T/p_g)$ is the air diffusion coefficient[26] and τ the tortuosity. The gradient of vapour density is approximated as[20]:

$$\operatorname{grad}\left(\rho_v\right) = \frac{\rho_0 M_w g RH}{RT}\operatorname{grad}\left(\frac{-s}{\rho_w g}\right) + RH\left[\frac{\partial \rho_0}{\partial T} + \frac{\rho_0 M_w}{\rho_w RT^2}\right]\operatorname{grad}\left(T\right) \tag{15}$$

where ρ_0 is the saturated density of water vapour RH is the relative humidity.

Heat transport is governed by both conduction and convection:

$$\mathbf{f}_T = -\Gamma\operatorname{grad}\left(T\right) + \left[c_{p,w}\rho_w \mathbf{f}_w + c_{p,a}\left(\mathbf{i}_a + \rho_a \mathbf{f}_g\right) + c_{p,v}\left(\mathbf{i}_v + \rho_v \mathbf{f}_g\right)\right]\left(T - T_0\right) \tag{16}$$

where Γ is the thermal conductivity of the mixture. In view of the available experimental results, Γ was considered as a volume average of the conductivities of each phase Γ_i:

$$\Gamma = \Gamma_s\left(1-n\right) + \Gamma_w S_r n + \Gamma_a\left(1-S_r\right)n \tag{17}$$

2.3. THM elastoplastic model of bentonite

An essential feature of the analysis presented concerns the THM stress–strain constitutive model for the bentonite behaviour. For this, the hydro-mechanical model presented in Ref. 18 is extended to non-isothermal conditions including thermoplasticity.

The total strain tensor $\boldsymbol{\epsilon}$ is divided into elastic and plastic strains:

$$\boldsymbol{\epsilon} = \boldsymbol{\epsilon}^e + \boldsymbol{\epsilon}^p \tag{18}$$

where the superscripts e and p denote elastic and plastic strains respectively. The following Bishop-type expression is used for the effective stress $\boldsymbol{\sigma}'$[27]:

$$\boldsymbol{\sigma}' = \boldsymbol{\sigma} - \left[p_a - \left(p_a - p_w\right)S_r\right]\mathbf{I} \tag{19}$$

where $\boldsymbol{\sigma}$ is the total stress tensor and p_a is the pore air pressure. The equations of the model are written in terms of the stress invariants $p' = \frac{1}{3}\operatorname{tr}\left(\boldsymbol{\sigma}'\right)$, $q = \sqrt{3}J$ and $\sin(3\theta) = 3\sqrt{3}\det \mathbf{s}/2J^3$, where $\mathbf{s} = \boldsymbol{\sigma}' - p'\mathbf{I}$ and $J = \sqrt{\frac{1}{2}\operatorname{tr}(\mathbf{s}^2)}$. Likewise, the strain invariants $\epsilon_v = \operatorname{tr}\left(\boldsymbol{\epsilon}\right)$ and $\epsilon_d = \sqrt{\frac{1}{3}\operatorname{tr}(\boldsymbol{\gamma}^2)}$, where $\boldsymbol{\gamma} = \boldsymbol{\epsilon} - \frac{1}{3}\epsilon_v\mathbf{I}$, are defined.

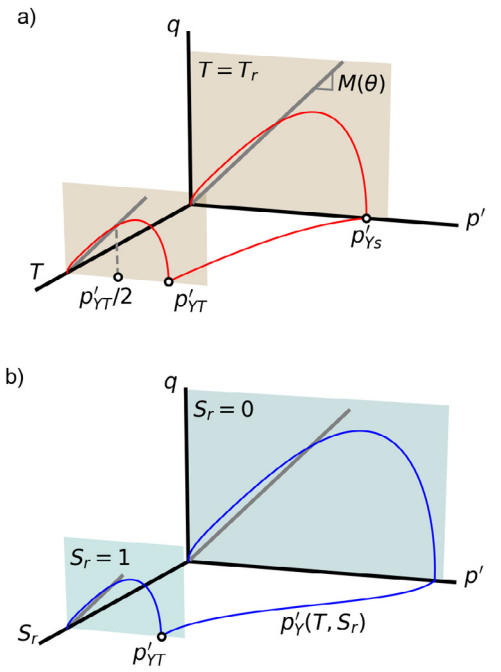

Fig. 2. Yield surface of the constitutive model in (a) the (p', q, T) space and (b) in the (p', q, S_r) space.

The elastic strains are related to changes in the effective stress and temperature, T according to:

$$\mathrm{d}\epsilon_v^e = \frac{p'}{\kappa}\mathrm{d}p' + \frac{1}{3}\left[\beta_{T0} + \beta_{T1}\left(T - T_r\right)\right]\mathrm{d}T, \tag{20a}$$

$$\mathrm{d}\epsilon_d^e = \frac{9\left(1-2\nu\right)}{2\left(1+\nu\right)}\frac{p'}{\kappa}\mathrm{d}q \tag{20b}$$

where κ is the elastic volumetric compressibility parameter, ν is the Poisson ratio, T_r is a reference temperature and β_{T0}, β_{T1} are thermo-elastic parameters.[28] The yield surface, f_Y in the stress space is defined after Ref. 29:

$$f_Y = q^2 - M^2\left[\alpha + \left(1-\alpha\right)\left(\frac{2p'}{p'_Y}\right)\right]^2\left(p'_Y - p'\right)p' = 0 \tag{21}$$

where M is the critical stress ratio, which depends on θ, α is a material parameter, and p'_Y corresponds to the yield pressure, which depends on the stress history and the current S_r and T. A dependency of strength on the stress path is established by taking the critical stress ratio as a function of $\sin(3\theta)$[30,31]:

$$M\left(\theta\right) = M_c\left[\frac{1 + b_L\sin\left(3\theta\right)}{1+b_L}\right]^{-0.229} \tag{22}$$

where b_L is defined as:

$$b_L = \frac{\left(M_c/M_e\right)^{1/-0.229} - 1}{\left(M_c/M_e\right)^{1/-0.229} + 1} \tag{23}$$

where $M_c = \frac{6\sin\phi'_c}{3-\sin\phi'_c}$, $M_e = \frac{6\sin\phi'_e}{3+\sin\phi'_e}$ and ϕ'_c and ϕ'_e are the shear strength angles at failure for compression paths and extension paths respectively.

The yield pressure, p'_Y depends on the degree of saturation according to:

$$\frac{p'_Y}{p'_r} = \left(\frac{p'_{TY}}{p'_r}\right)^{\frac{\lambda_s-\kappa}{\lambda(S_r)-\kappa}} \tag{24}$$

where p'_{TY} is the saturated yield pressure at current temperature, p'_r is a reference stress, λ_s defines the elastoplastic compressibility during yielding for saturated states and $\lambda\left(S_r\right)$ is a function expressing the evolution of elastoplastic compressibility with the degree of saturation, using a modified version of the expression proposed by Zhou et al.[32]:

$$\lambda\left(S_r\right) = \lambda_s - r\left(\lambda_s - \kappa\right)\left(1 - S_r^{\zeta}\right)^{\xi} \tag{25}$$

where r, ζ and ξ are material parameters that generally depend on the initial compaction state. The dependency of yield on temperature is introduced after Ref. 33 and Ref. 28:

$$p'_{TY} = p'_{Ys}\left[1 - \gamma_T\ln\left(\frac{T}{T_r}\right)\right] \tag{26}$$

where p'_{Ys} is the hardening variable (corresponding to the yield pressure at $S_r = 1$ and $T = T_r$ for a fixed ϵ_v^p) and γ_T is a material parameter. A graphical representation of the yield surface in the $\left(p', q, T\right)$ and $\left(p', q, S_r\right)$ planes is shown in Fig. 2.

Volumetric and deviatoric plastic strain increments are given by the following flow rule[29]:

$$\frac{\mathrm{d}\epsilon_d^p}{\mathrm{d}\epsilon_v^p} = \frac{q}{M^2\left(p' - p'_Y/2\right)\left[\alpha + \left(1-\alpha\right)\left(\frac{2p'}{p'_Y}\right)\right]^2} \tag{27}$$

p'_{Ys} evolves according to the hardening law:

$$\frac{\mathrm{d}p'_{Ys}}{p'_{Ys}} = \frac{\mathrm{d}\epsilon_v^p}{\lambda_s - \kappa} \tag{28}$$

The water retention model is formulated in terms of the water ratio, e_w (ratio of water volume with respect to volume of solids) which is divided into free water ratio, $e_{w,f}$ (volume of non-adsorbed water with respect to volume of solids) and adsorbed water, $e_{w,a}$ (volume of adsorbed water with respect to volume of solids) i.e., $e_w = e_{w,f} + e_{w,a}$. The degree of saturation is computed as $S_r = e_w/e$. The evolution of free water ratio $e_{w,f}$ is modelled using a similar expression to that proposed by Dieudonne et al.[16] as:

$$e_{w,f} = \left(e - e_{w,a}\right)\left[1 + \left(a\left(e - e_{w,a}\right)^b s\right)^n\right]^{1/n-1} \tag{29}$$

where n, a and b are material parameters and s stands for matric suction. $e_{w,a}$ follows a Freundlich isotherm[34]:

$$e_{w,a} = e_{w,a}^C\left[\exp\left(-\frac{M_w}{\rho_{w,a}RT_r}s\right)\right]^{1/m} \tag{30}$$

where $\rho_{w,a}$ is the density of adsorbed water, $e_{w,a}^C$ is the adsorption capacity parameter and m is a material parameter. Note that while free water ratio depends on the current void ratio, the adsorbed water ratio depends solely on suction. The water content is computed accounting for the differences between the free water density $\rho_{w,f}$ and adsorbed water density $\rho_{w,a}$:

$$w = \frac{1}{\rho_s}\left(\rho_{w,f}e_{w,f} + \rho_{w,a}e_{w,a}\right) \tag{31}$$

In the present study no variations of the water retention behaviour with temperature were considered. The constitutive model has been implemented in the FEM code Lagamine. The numerical integration is performed using an extension of the explicit schemes with automatic error control proposed by Sloan[35] and Sheng et al.[36], incorporating S_r and T as stress-like variables.

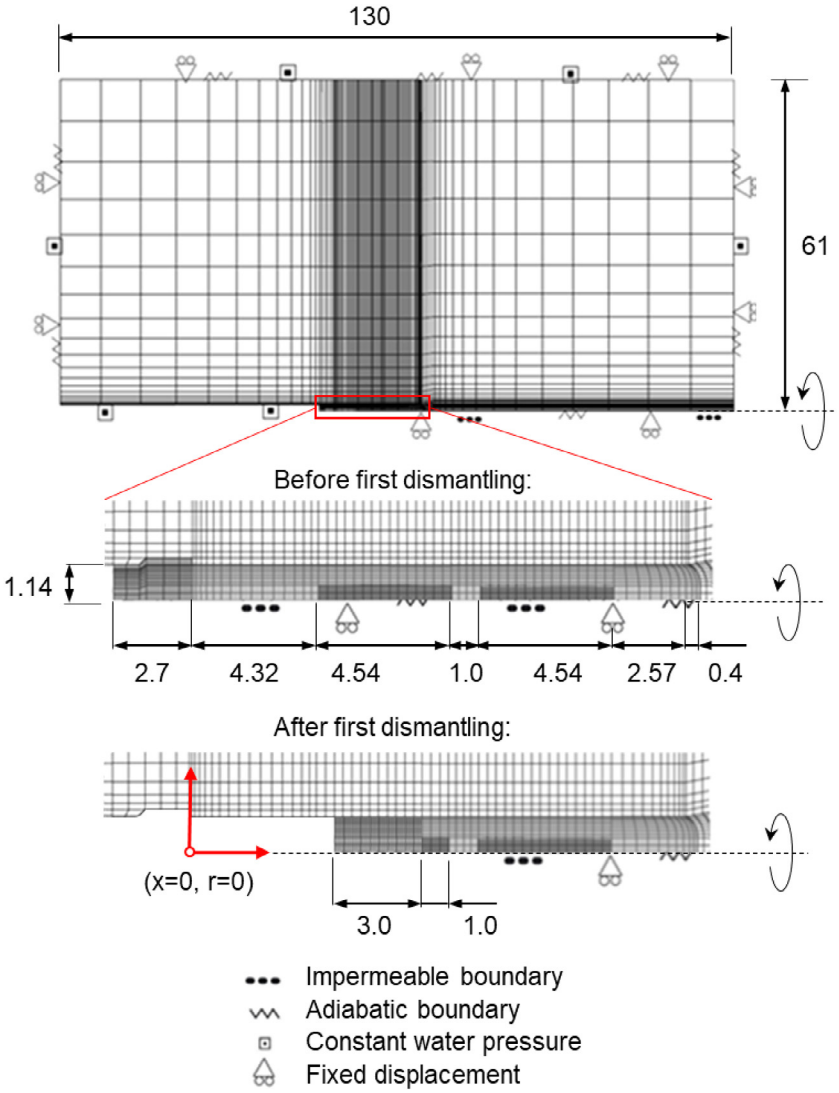

Fig. 3. Axisymmetric geometry and finite element mesh used in the analysis before and after the first partial dismantling. All units are in meters.

3. Finite element model

3.1. Geometry, discretisation and boundary conditions

Fig. 3 shows the geometry, discretisation and boundary conditions used in the finite element model. In order to avoid undesired effects of the imposed boundary conditions, the distance of the external boundary to the engineered barrier is located at 60 m in both the axial and radial directions. The test is modelled as an axisymmetric problem. The perpendicular displacements of all boundaries are prevented, except for the gallery surface of the service tunnel. Based on in situ measurements an initial isotropic total stress of 28 MPa was assumed for the granite. The initial water pressure and temperature are also assumed to be uniform with $p_w = 0.7$ MPa and $T = 12$ °C, and are fixed at the external boundaries. Perfect contact is assumed between all materials.

The phases considered in the simulation of the experiment are summarised in Table 1, where day 0 corresponds to the time at which the heaters were switched on. The excavation process is simulated by releasing the radial stress at the tunnel walls to 0 MPa during the first 35 days. The ventilation process is simulated by setting the water pressure of the drift surface to atmospheric pressure for 243 days. Subsequently, the bentonite buffer construction, canister installation and plug construction are modelled by activating the bentonite, canister and plug elements. Given the relative humidity measured at the beginning of the test, an initial suction of 130 MPa is considered for the bentonite buffer. Initially, no external total stress is applied on the bentonite.

The temperature increase sequence involved a first stage of 1200 W per heater for 20 days and subsequently 2000 W per heater over the following 33 days until reaching the target temperature of 100 °C. The thermal losses due to the presence of air in the construction gaps between the heaters and the bentonite were estimated at 15%.[10] Accordingly, the power applied in the simulation is 85% of the real power. After the temperature of the heater centre reached 100 °C, the temperature on all heater nodes (both heater #1 and #2) is kept constant. After 1826 days of heating, the power in heater #1 is switched off. The dismantling process is simulated by switching off the plug, bentonite and canister elements from the model domain, following the same sequence of the dismantling plan. The second plug construction is simulated by activating concrete plug elements in which the initial water pressure is assumed to be at the atmospheric pressure. After 6607 days of heating, heater #2 is switched off. The

Table 1
Stages of the FEBEX test included in the analysis.

Phase	Start time	Task	Starting day (ref.)
–	25/09/1995	TBM excavation of FEBEX tunnel – excavation: 35days – ventilation period: 243 days	−520
–	01/07/1996	EBS construction and emplacement of heaters	−242
A	15/10/1996	End of EBS construction	−135
B	28/02/1997	Heating at constant power – 1200 W from 0 to 20 days – 2000 W from 20 to 53 days	0
C	21/4/1997	Heating (Constant temperature)	53
D	28/02/2002	Switch off Heater #1	1826
E	02/04/2002	Start of partial dismantling	1859
F	26/07/2002	Shotcrete plug construction	1975
G	2/04/2015	Switch off Heater #2	6607
H	21/07/2015	End of dismantling	6717

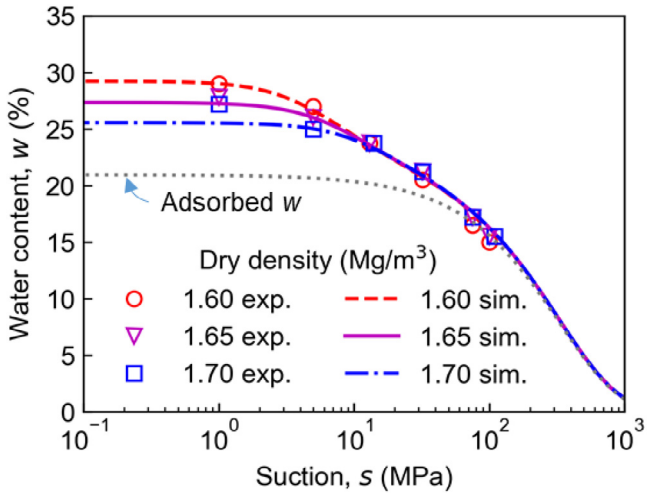

Fig. 4. Water retention model calibration (denoted by sim.) against the experimental results obtained by Lloret et al.[4] upon wetting paths (denoted by exp.).

sequence used in the final dismantling is analogous to the one used in the first dismantling phase, finishing at day 6717.

3.2. Determination of FEBEX bentonite material parameters

In addition to control the hydraulic conductivity and thermal conductivity, S_r is one of the main state variables used in the mechanical constitutive model through the adopted effective stress form. Therefore, the water retention curve was calibrated prior to calibrate the mechanical parameters. The data presented by Ref. 4, shown in Fig. 4, was used to calibrate the water retention parameters. The tests consisted in wetting paths, performed at ambient temperature under constant volume conditions at different dry densities that are representative of the EBS of the FEBEX test. The two parameters of the adsorbed water content ($e^C_{w,a}$, m) were found by fitting the curve to the high-suction range, where water content is rather independent on dry density.[37] Adsorbed water might present densities that are higher than those of free water.[38] In this case in order to match the water contents at low values of suction, the adsorbed water density was set to 1.2 Mg/m^3 which is in line with previous studies.[39] The simulated adsorbed water content is also shown in Fig. 4. No dependency of water retention properties on temperature were considered in the analysis, as its effect was shown to be small experimentally by Villar and Lloret[40] and numerically by Dupray et al.[10] Experiments by Villar[41] showed a negligible retention hysteresis at high suction, and since drying paths are only expected close to the heaters at high suctions, hysteresis was neglected in the analysis.

The isothermal elastoplastic parameters were calibrated based on the suction-controlled oedometric tests reported by Lloret et al.[4] shown in Fig. 5. The initial state of the samples was characterised by a high compacted state with a void ratio of $e = 0.58$, a suction around 127 MPa and a low axial stress of $\sigma_a = 0.1$ MPa. These tests span several ranges of suction-stress values, following two stress paths that are relevant in an EBS. Both tests involved a first drying to high suction of $s = 550$ MPa, prior to be compressed and then saturated (test S1) and saturated and then compressed (test S5). Although they were conducted under iso-thermal conditions, both stress paths can be representative of the bentonite inside a repository, where the high suction will be the result of the heating induced drying and the compression will be induced by the neighbouring bentonite elements as they progressively saturate. In the case of the inner bentonite, the compression would be induced at high suction (test S1) and for the outer bentonite, the compression stage would happen at low suctions (test S5). The model is able to reproduce consistently the results of both tests. The assumption of neglecting hysteresis in the high suction range is also accepted in view of the good fit that is obtained in the drying-wetting cycle of the test S5 (path A-B'-C'). Shear strength angle was derived from the values reported in Ref. 42. All input parameters used to simulate these tests, are reported in Table 2 ($e_0 = 0.58$).

Lloret et al.[4] highlighted the stress path dependent behaviour of the bentonite that is observed in tests S1 and S5. Indeed, although the initial and final stress-suction states were the same in both samples, the final void ratio is different. While the experimentally controlled variables are the total stress and suction, the constitutive variables of the model are the generalised effective stress and the degree of saturation, which unify the interpretation across different saturation states. Therefore it is worth examining the model results in terms of the constitutive variables (p', e, S_r) as shown in Fig. 6, as it supports an explanation to the final state of the bentonite barrier of the FEBEX test that is discussed in Section 4.3. The initial state (point A) is characterised by the high p' arising from the high product sS_r. Upon drying to points B and B', p' does not increase due to the large decrease in S_r, which naturally results into a shrinkage limit. The suction decrease stages, CD and B'C', involve an increase in S_r that eventually implies reaching the loading collapse yield curve, which

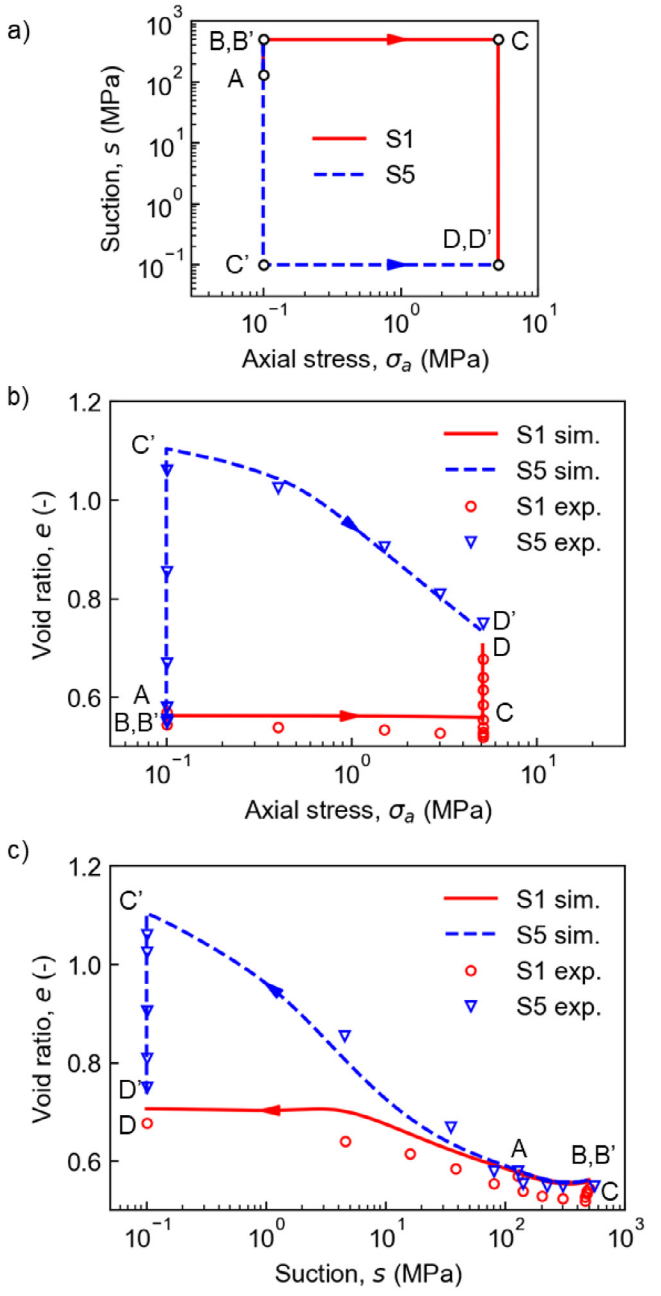

Fig. 5. Calibration (denoted by sim.) of the iso-thermal mechanical parameters of FEBEX bentonite upon stress and suction changes against the experimental data reported by Lloret et al.[4] (denoted by exp.). (a) suction-stress paths. (b) Response in the (σ_a, e) plane. (c) Response in the (s, e) plane.

happens at a larger value of suction in test S1 as a result of the higher axial stress applied during wetting. The higher axial load involves higher plastic strains owing to the lower swelling and thus to the faster increase in S_r compared with test S5 where S_r increases slower due to the lower axial stress that allows significant swelling, leading to smaller plastic strains during wetting. After compression, the sample S5 does not reach the void ratio at which S5 equilibrated after wetting due to the different sequence of plastic strains between the tests. Both tests resulted in stress states located close to the normal compression line at saturation defined by λ_s. Thus, the Febex bentonite response can also be interpreted using hydro-mechanical coupling effects, as an alternative to a double porosity model.

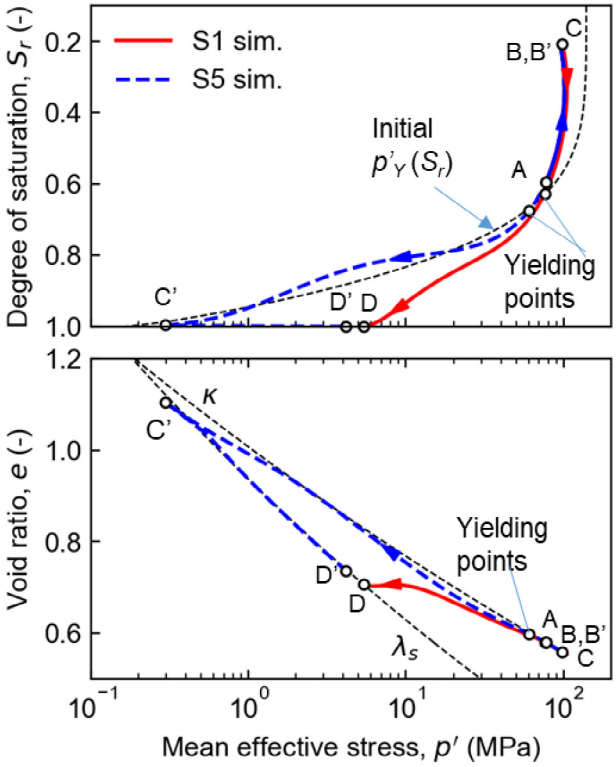

Fig. 6. Model simulation of tests S1 and S5 in terms of constitutive variables (p', S_r, e).

Table 2
THM constitutive parameters for the FEBEX bentonite. (1) corresponds to an initial void ratio $e_0 = 0.58$, whereas (2) corresponds to an initial void ratio of $e_0 = 0.70$.

Mechanical model		Water retention model	
Parameter	Value	Parameter	Value
κ	0.055	a	2 MPa^{-1}
ν	0.35	b	1.5
λ_{sat}	0.075	n	1.8
$\phi'_c = \phi'_e$	16°	m	2.5
α	0.65	$e^C_{w,a}$	0.48
p'_r	10^{-7} MPa	$\rho_{w,a}$	1.2 Mg/m^3
r	0.320 (1), 0.525 (2)		
ζ	5.50 (1), 3.17 (2)		
ξ	0.80 (1), 1.65 (2)		
β_{T0}	1.8 × 10 $^{-4}$/°C		
β_{T1}	0		
γ_T	0.25		
T_r	20 °C		
e_0	0.58 (1), 0.70 (2)		

It is noted that while the bentonite blocks that constitute the buffer have a dry density of 1.7 Mg/m^3 the overall dry density of the buffer is 1.6 Mg/m^3, that is considering technological gaps between the blocks, tunnel and heaters. As an alternative to modelling explicitly these gaps, the present analysis considers an overall equivalent dry density. This assumption provided reasonable results in previous studies[6,10] and it is supported by the results of laboratory tests performed by Wang et al.[43] who observed a unique relationship between the swelling pressure and the overall dry density considering different gap volumes. Accordingly, the initial dry density of the bentonite elements is set as 1.6 Mg/m^3, homogeneously distributed throughout the EBS.

In order to account for the difference between the initial density of the overall barrier and the oedometric tests, the

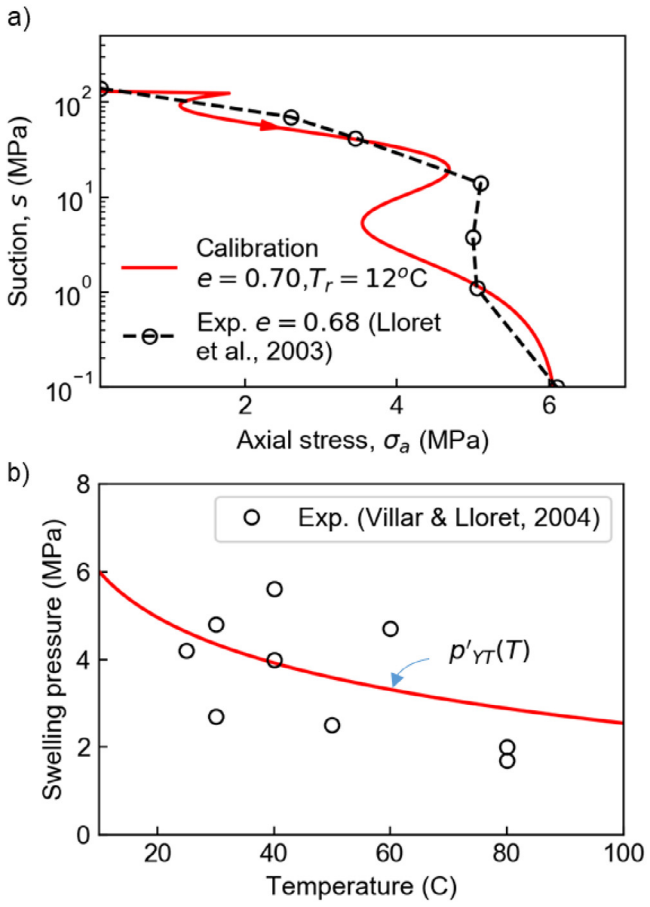

Fig. 7. Adjustment of the model parameters against swelling pressure tests. (a) Calibration of r, ζ and ξ for an initial $e = 0.7$ against experimental data by Lloret et al.[4] (b) Calibration of the γ_T and T_r with swelling pressure results reported by Villar and Lloret[40] at an average dry density of 1.58 Mg/m^3.

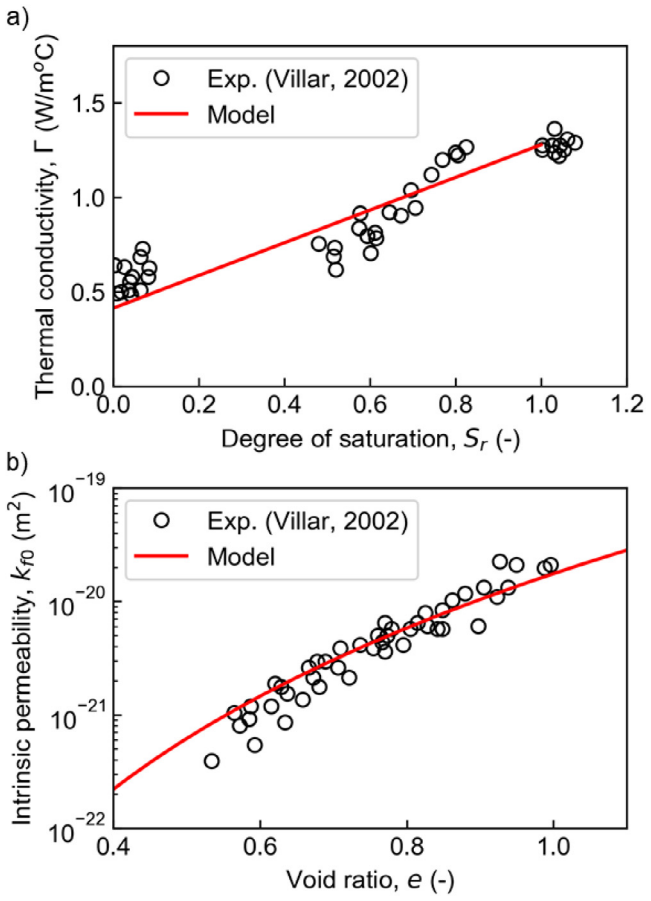

Fig. 8. (a) Calibration of the thermal conductivity and (b) calibration of the dependency of intrinsic permeability on void ratio. All the experimental data was reported by Villar.[41]

parameters r, ζ and ξ, which depend on the initial compaction state, are adjusted. They have been independently calibrated against a suction-controlled swelling pressure test reported by Ref. 4, performed at ambient temperature with a dry density close to 1.6 Mg/m^3. Fig. 7a shows both the experimental results and the model calibration with the parameters reported in Table 2 for $e_0 = 0.70$. The swelling pressure evolution (in terms of axial stress) with suction is captured fairly well although the coupling between the loading collapse curve and the water retention in the model results in a nonlinear development of swelling pressure. While the development of swelling pressure during wetting is determined by ξ and ζ, the model predicts that at $s = 0$ the swelling pressure is given by the λ_s-line. This can be verified observing that the value of $p' = 6$ MPa in the λ_s-line plotted in Fig. 5 corresponds to $e = 0.70$, i.e. a dry density of 1.6 Mg/m^3.

In line with the above result, experimental evidence suggests that the decreasing trend of swelling pressure on temperature can be explained by means of the dependency of yield pressure on temperature.[44] Accordingly, the thermal yield, which defines the position of the λ_s-line at different temperatures (Eq. (24)), is calibrated on the basis of the swelling pressure results presented by Ref. 40, who observed a logarithmic decrease of swelling pressure with increasing temperature. The experimental results (with an average dry density of 1.58 Mg/m^3) and the model calibration are shown in Fig. 7b. In spite of the scattering of experimental data, a value of $\gamma_T = 0.25$, and $T_r = 12\ ^\circ C$ follows the decreasing trend of swelling pressure with temperature.

Fig. 8a shows the calibration of the thermal conductivity of bentonite against experimental data from Ref. 41 for various S_r. Using Eq. (15), a good match is obtained with $\Gamma_s = 0.7$ W/m°C and $\Gamma_w = 2.1$ W/m°C, considering $\Gamma_a = 0$. Villar[41] also reported the intrinsic permeability for a wide range of void ratios, which is reproduced in Fig. 8b together with the fit of k_{f0} that is obtained with $MKC = 6$ and $NKC = 4$. The dependency of k_{rw} on S_r is accounted by using Eq. (10) with $\alpha_k = 3$ as proposed by Pintado et al.[45] All the input THM material parameters of the bentonite are summarised in Table 2. The remaining water and heat flow parameters have been derived from the previous study by Dupray et al.[10] and they are summarised in Table 3.

3.3. Granite, steel and concrete parameters

The granite is assumed to be fully saturated throughout the analysis and its mechanical behaviour is considered linear elastic, defined by the Young modulus E and Poisson ratio ν, on the basis of laboratory results from early studies in the Grimsel laboratory.[46] The parameters of the steel heaters, as well as the concrete plug, have been set in the range of usual parameters from previous studies (e.g. Ref. 10). Their mechanical behaviour is also modelled as linear elastic. The steel is considered as impermeable and the concrete plug as fully saturated. The mechanical, thermal and hydraulic parameters of the granite, steel and concrete are summarised in Table 3.

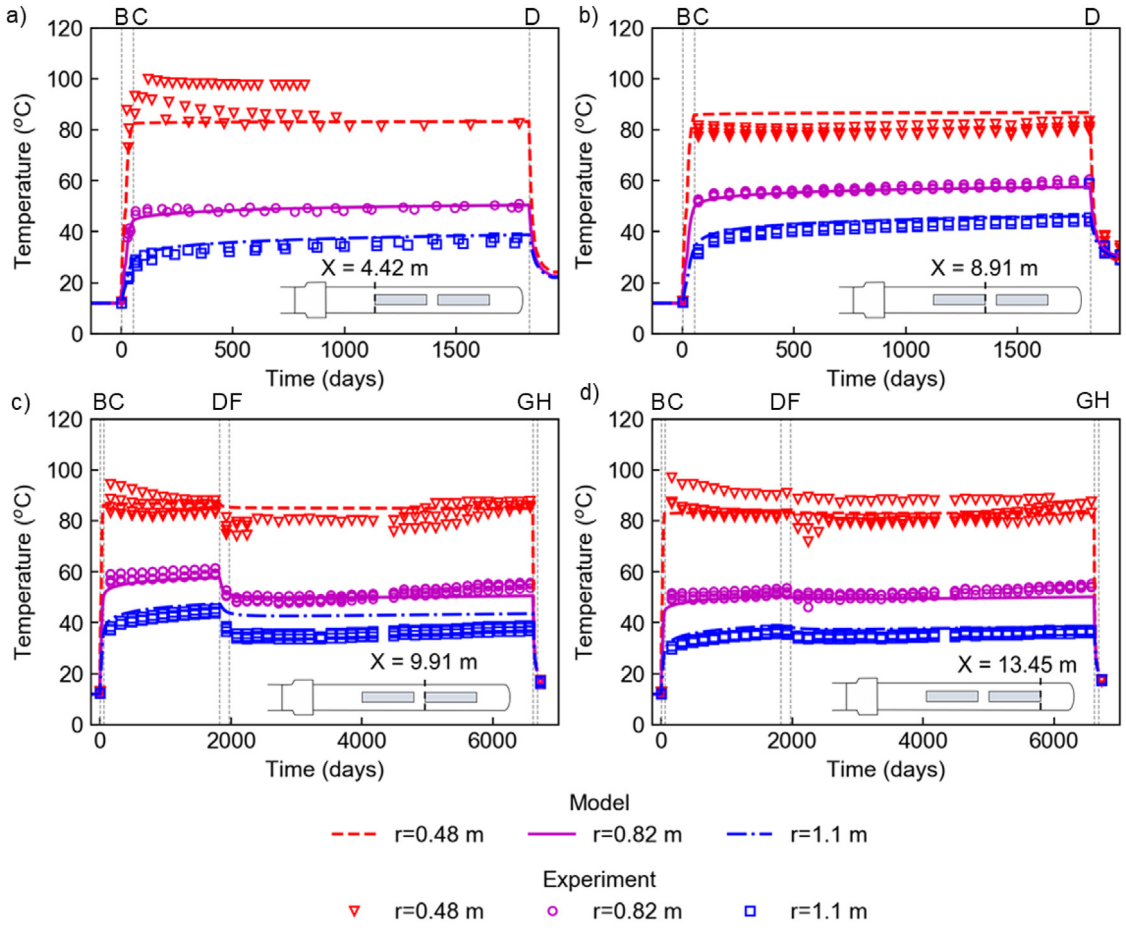

Fig. 9. Model and experimental results in terms of temperature at four sections. (a) x = 4.42 m (until first dismantling); (b) x = 8.91 m (until first dismantling); (c) x = 9.91 m and (d) x = 13.45 m. The capital letters and the corresponding dashed lines indicate the different phases described in the text.

Table 3
Water and heat flow parameters for the bentonite, granite, concrete and steel.

Parameter	Bentonite	Granite	Concrete	Steel
Γ [W/(m°C)]	–	3.34	1.7	52
c_p [J/(kg°C)]	–	1000	750	500
p_{w0} [MPa]	0.1	0.1	0.1	–
χ_w [1/Pa]	4.4×10^{-10}	4.4×10^{-10}	4.4×10^{-10}	–
β_w [1/°C]	4×10^{-4}	4×10^{-4}	4×10^{-4}	–
$k_{f,0}$ [m^2]	3×10^{-21} m^2	4.5 × 10–19	4 × 10–19	–
τ [–]	0.5	0.6	0.6	–
n_0 [–]	See e_0 in Table 1	0.01	0.15	–
ρ_s [kg/m^3]	2720	2660	2500	7800
E [GPa]	–	50	30	200
ν [–]	–	0.35	0.2	0.3
Γ_s [W/(m°C)]	0.7 W/(m°C)	–	–	–
Γ_w [W/(m°C)]	2.1 W/(m°C)	–	–	–
Γ_a [W/(m°C)]	0	–	–	–
$c_{p,s}$ [J/(kg°C)]	1091	–	–	–
$c_{p,w}$ [J/(kg°C)]	4183	–	–	–
$c_{p,a}$ [J/(kg°C)]	1000	–	–	–
H	0.017	0.017	0.017	–
MKC	6	–	–	–
NKC	4	–	–	–
α_k	2.9	–	–	–

4. Model results and interpretations

4.1. Temperature, relative humidity and stresses

In the following, the model results are compared to the temperature, relative humidity and total stresses measured during the test operation, focusing on the EBS. Sections corresponding to the first heater comprise the first 5 years of operation and sections corresponding to the second heater involve data spanning 18 years. The sections are defined by their distance, x, to the initial concrete plug. Capital letters in the Figures relate to the different stages of the test as defined in Table 1.

The evolution of temperature is shown in Fig. 9 for the four sections located at the edges of the heaters at different radial distances. The experimental data is well captured by the model, including the cooling phase (starting at D) induced by switching off the heater #1 at day 1826. This effect can be well appreciated in section x = 8.91 m before the first dismantling. After the first dismantling, the temperature values in section x = 9.91 m stabilised at a lower temperature until the end of the test. The temperature at x = 13.45 m was slightly affected close to the host rock (r=1.1 m) when the heater #1 was switched off (denoted by D). The results in terms of relative humidity are shown in Fig. 10 (sections before the first dismantling) and Fig. 11. In spite of the higher scattering of the experimental data, it can be observed that the model captures the general trend of hydration and drying. At the points close to the host rock (i.e. close to $r = 1.14$ m) a fast increase in *RH* occurs as soon as the EBS is emplaced. The increase of *RH* close to the host rock in the hot section (x = 6.69 m in Fig. 10b) when heater #1 is switched on (B) is noticeable compared to the negligible effect that it has on the cold section (x = 1.80 m, Fig. 10a). This increase is due to the vapour transfer induced by the significant thermal gradient. The first dismantling (D) has a clear effect on the trend of *RH* modelled in the section between the two heaters (x = 9.5 m in Fig. 11a), whereas it has

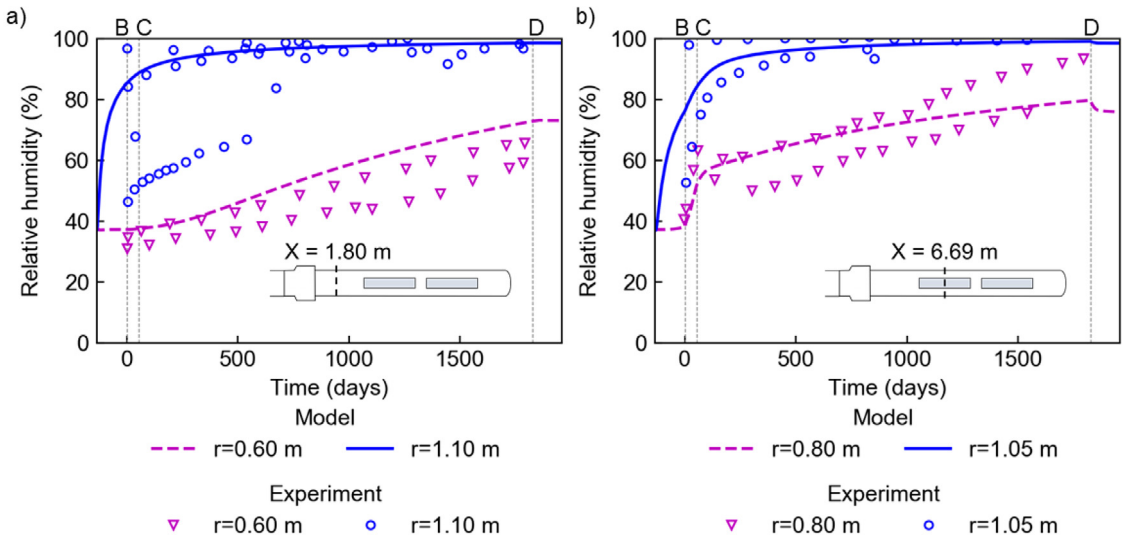

Fig. 10. Model and experimental results in terms of relative humidity at two sections until the first dismantling. (a) x = 1.80 m and (b) x = 8.91 m. The capital letters and the corresponding dashed lines indicate the different phases described in the text.

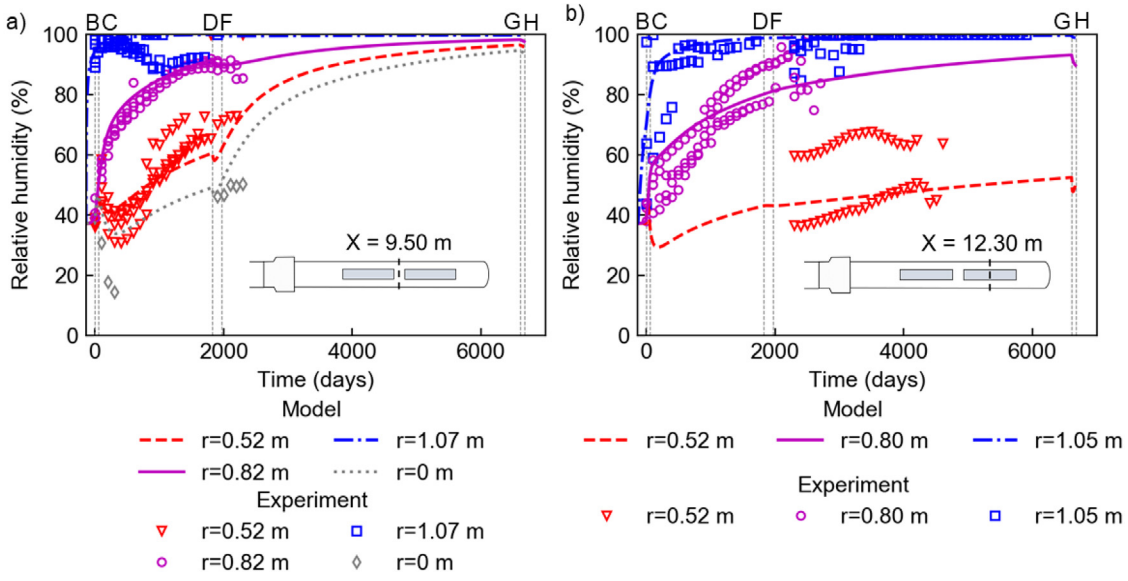

Fig. 11. Model and experimental results in terms of relative humidity at two sections. (a) x = 9.50 m and (b) x = 12.30 m. The capital letters and the corresponding dashed lines indicate the different phases described in the text.

a very limited effect on the evolution of *RH* in the hot section at x = 12.3 m (Fig. 11b). Although the available data of *RH* after the first dismantling is not as extensive as during the first years a similar trend is followed by the model.

The performance of the proposed THM constitutive model can be evaluated from the results in terms of total stresses that are shown in Fig. 12 (radial stresses) and in Fig. 13 (axial stresses), at different sections. While the precision of the measurements in terms of stresses is not high[47] they give an overall idea of the trend and the order of magnitude of pressure changes. The initial increase in stress predicted by the model in all sections is due to the hydration of the bentonite, that in the model is assumed to be in full contact with the host rock. Afterwards, the increase of temperature (B) in the hot sections (Figs. 12 and 13b) induces a stress decrease that is related to the suction increase and the coupling between yield pressure and temperature, according to the model hypothesis that the thermal yield controls the dependency of swelling pressure on temperature (see Fig. 7b). As the hydration front advances, the swelling pressure increases again up to the point in which the heater #1 is switched off (D). The decrease in temperature induces a stress unloading, in agreement with the data monitored in the two sections corresponding to the heater #1 (Figs. 12a and 12b). In that case the stress decrease is due to the elastic contraction of the material. While the magnitude of stresses around heater #2 (Figs. 12c and 12d) is fairly well predicted, it develops a different radial trend to that measured in the test, which could be consequence of a poor contact between the sensors and the heater induced by the strong drying of bentonite.[3]

In terms of axial stress (Fig. 13) the model also captures the overall trend of swelling pressure increase, although with a lower axial stress than that measured in the test. It is of particular interest the stress build-up monitored in the shotcrete plug (Fig. 13b) that is well predicted by the model. This indicates

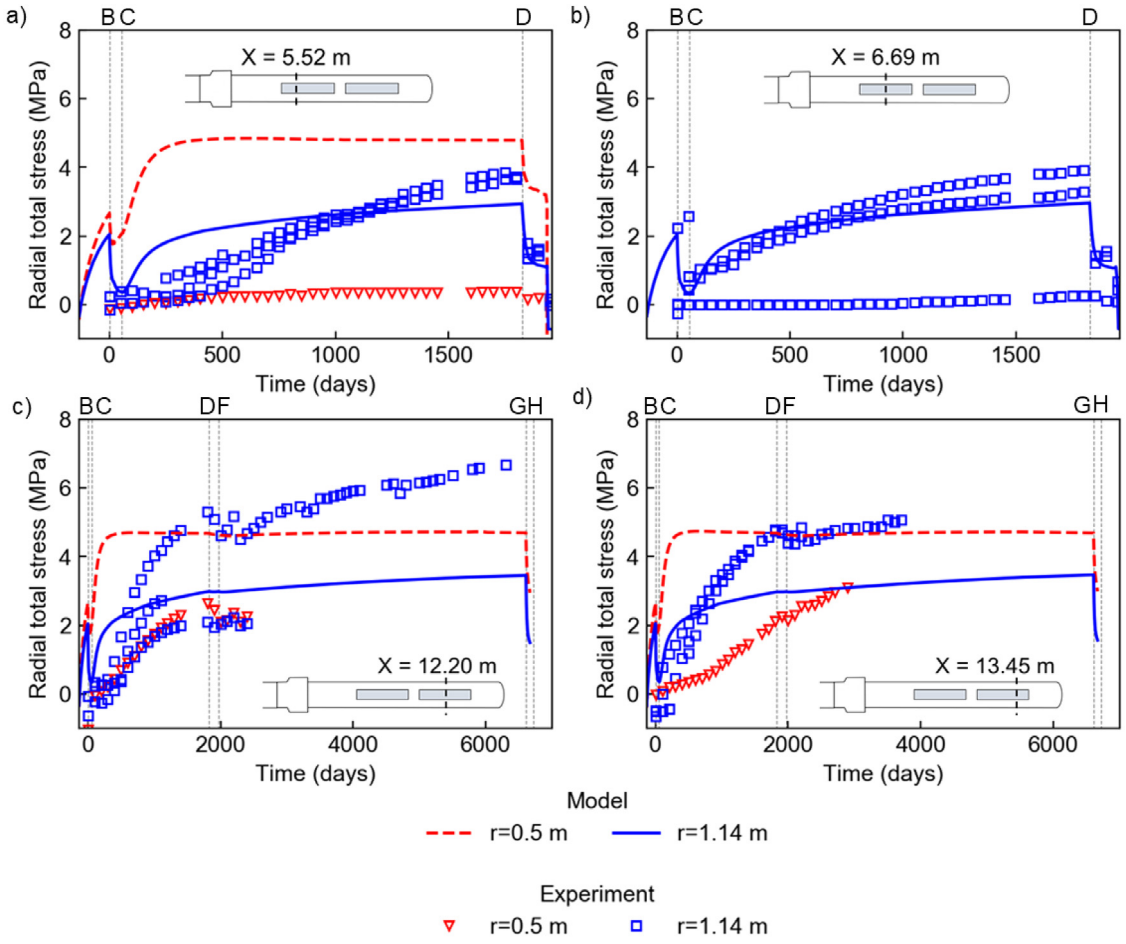

Fig. 12. Model and experimental results in terms of total radial stresses at four sections. (a) x = 5.52 m (until first dismantling); (b) x = 6.69 m (until first dismantling); (c) x = 12.20 m and (d) x = 13.45 m. The capital letters and the corresponding dashed lines indicate the different phases described in the text.

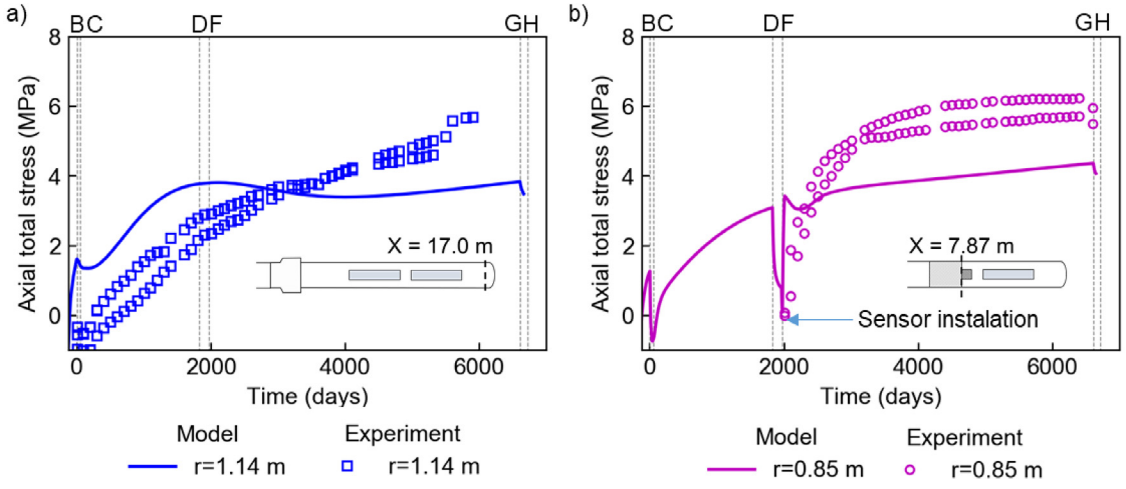

Fig. 13. Model and experimental results in terms of total axial stresses at two sections: (a) x = 17. 0 m and (d) x = 7.87 m. The capital letters and the corresponding dashed lines indicate the different phases described in the text.

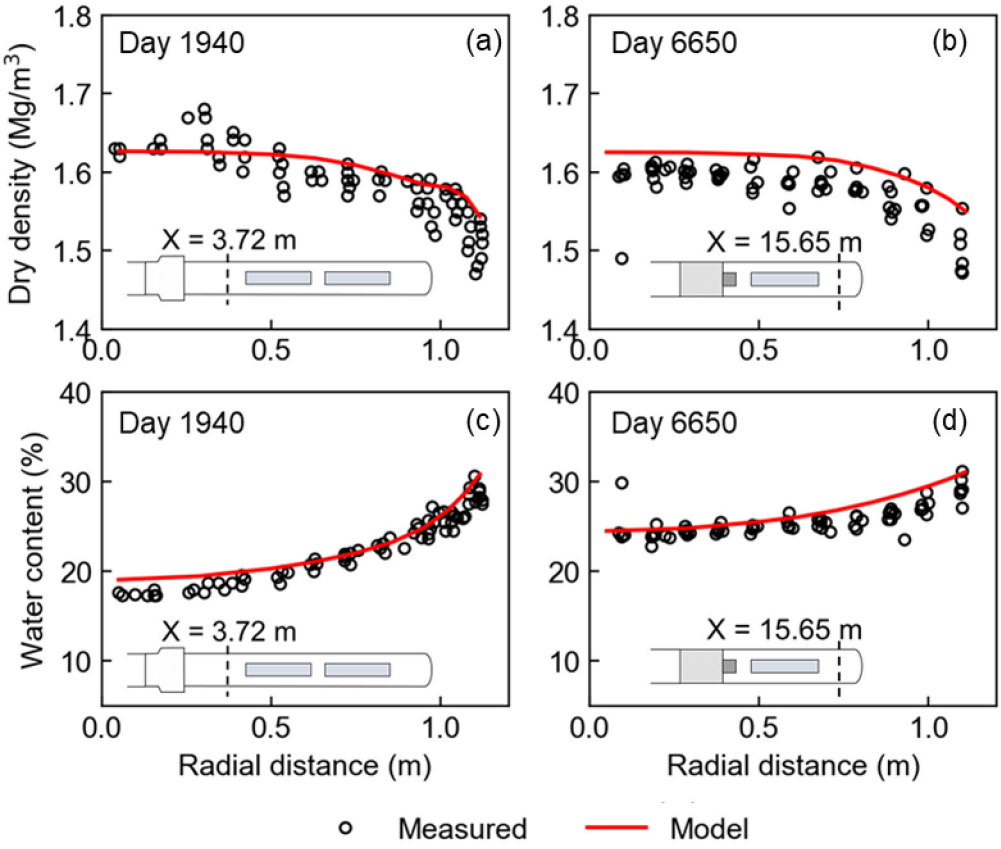

Fig. 14. Post-mortem results in cold sections in terms of dry density and water content after the first dismantling (a), (c) and second dismantling (b), (d).

a good capability of the constitutive model to reproduce the unloading–reloading behaviour of the bentonite in which thermal cycles are involved.

4.2. Post-mortem results

The post-mortem measurements after each dismantling stage allows the model performance to be evaluated in terms of water content and dry density. In this way, the complete stress–strain relation can be validated. Fig. 14 shows the dismantling and simulated results of two cold sections, one analysed after the first dismantling and the other after the second dismantling. The simulation results of the first dismantling correspond to the dry density after the concrete plug was removed, which induced an axial unloading, whereas the results of the second dismantling correspond to the removal of the second shotcrete plug. In both cases the modelling results are in good agreement with the trend of the experimental data, in particular with the water content measurements, which showed a lower degree of scattering compared to the results in terms of dry density. When comparing the results of the final dismantling with the partial dismantling, the water content increased mostly in the inner part of the buffer, while it remained fairly constant near the host rock. In spite of the 13 years that elapsed between the two dismantling stages, the two sections revealed a very similar gradient of dry density, slightly lower in the case of the second dismantling.

Fig. 15 shows the results of the dry density and water content distributions at two symmetrical hot sections, one corresponding to the first dismantling and the other to the second dismantling (data from Ref. 48). The modelling results match quite well the trends in experimental data close to the host rock, whereas they slightly deviate close to the heater. Although it evolved significantly with respect to the relatively homogeneous state, the dry density did not change significantly between the two dismantling stages, which is in line with the trend experienced by the cold sections. Also in these sections, the water content increased mostly towards the inner parts of the buffer, while decreasing slightly at the contact with the host rock, due to the compression originated by the swelling of the inner parts.

4.3. Interpretation of the THM stress paths

The final dry density observed after the post-mortem analysis showed a heterogeneous distribution of dry density of the barrier, which did not differ significantly between symmetrical sections analysed at each dismantling stage. In view of the consistency between the model performance for both laboratory and large-scale tests, the stress path of the bentonite in the EBS predicted by the numerical analysis is interpreted in order to offer an explanation and to identify a possible source of the heterogeneity.

The stress paths in terms of the constitutive variables (p', S_r, e, T) in a hot and a cold section are shown in Fig. 16. For each section, the points located at $r = 1.11$ m and $r = 0.5$ m are represented. The general trend is given by a decrease of p' induced by the decrease of sS_r upon hydration. It can be observed that the initial hydration that takes place between the bentonite emplacement (A) and the start of heating (B) already induces a decrease in p' at $r = 1.11$ m larger than that occurring in 18 years

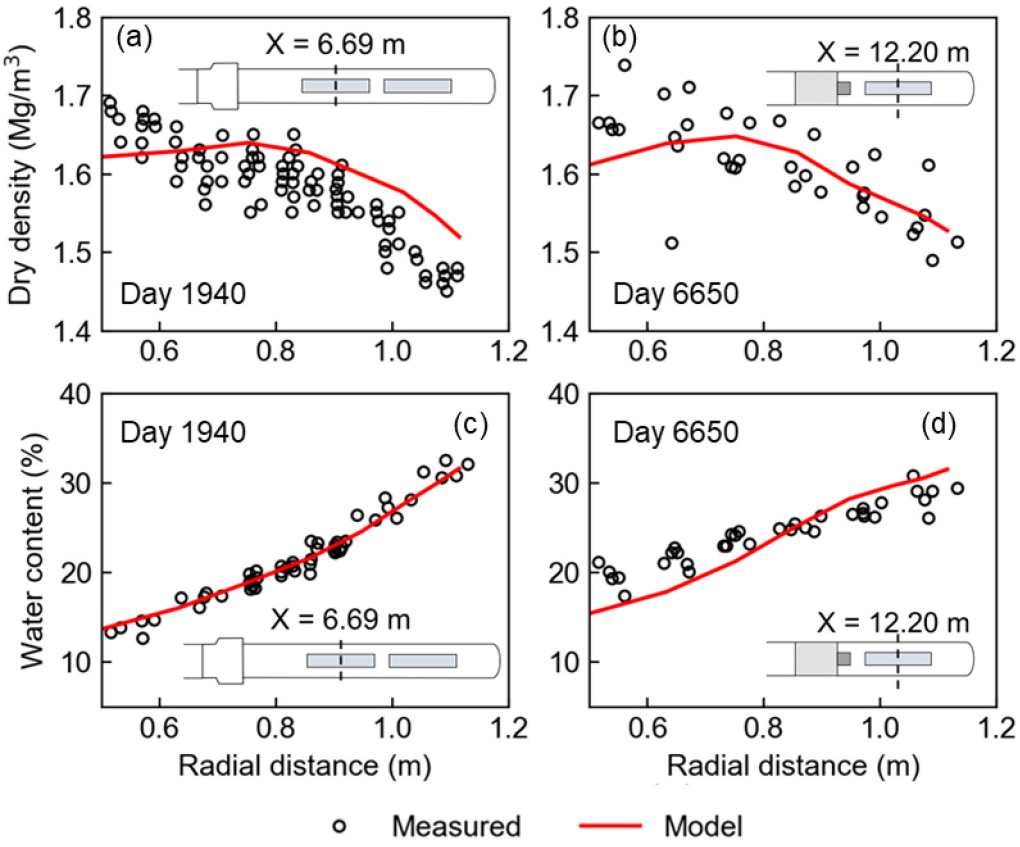

Fig. 15. Post-mortem results in hot sections in terms of dry density and water content after the first dismantling (a), (c) and second dismantling (b), (d).

at $r = 0.5$ m. This initial decrease reaches the initial LC curve in the plane $(p' - S_r)$ which implies an increase of plastic strains and thus the void ratio does not evolve following the κ-line (which represents purely elastic swelling). The differences between the hot and cold section are obviously due to the heating starting at point B. The stress path is significantly modified in the hot section at B because of temperature and there is a reversal in the stress path in plane (p', S_r) inside the elastic domain and thus e evolves following the κ-line. This is due to the drying occurring at $r = 0.5$ m, that densifies the bentonite close to the heater allowing the outer bentonite to swell under low external confinement. Although limited, this short elastic response results in a difference in void ratio between the hot and cold sections that persists until the end, adding up to the higher vapour transport that leads to different values of s. Note that this gradient does not tend to homogenise upon saturation, given that the plastic strains developed in the inner and outer radius differ as a result of the different stress sequence that occur. It is also observed that the λ_s-line determines the stress-state upon saturation, indicating the importance of calibrating its position (see Fig. 5) to obtain reliable predictions, in agreement with recent studies.[18,49]

The stress paths are in line with the results obtained in the suction-controlled oedometric tests (Figs. 5 and 6). The test S1, whose stress path was closer to an element close to the heater, equilibrated at a void ratio lower than the test S5, that followed a stress path more similar to that obtained in the contact with the host-rock.

Finally, the water retention behaviour in terms of S_r, resulting from the simulation in each of the four points represented in Fig. 16, is shown in Fig. 17. Note that the high density assumed for adsorbed water leads to an initial $S_r = 0.48$ lower than $S_r = 0.55$ that would result from considering an overall $\rho_w = 1$ Mg/m^3. Despite the confined nature of the overall EBS, the local water retention curve develops differently in each of the four points studied, hence the importance of considering a dependency of void ratio in order to predict the evolution of water content and the degree of saturation.

5. Conclusions

This study provided an interpretation of the final heterogeneous state of the bentonite barrier (EBS) in the FEBEX in-situ test by simulating its complete history with an advanced THM elasto-plastic stress–strain model for bentonite. The main novelty with respect to previous studies is the consideration of a two-way coupling between the water retention and volume change response of bentonite, including the explicit distinction between the behaviour of adsorbed water and free water. Thermo-plasticity is also incorporated allowing to model the dependency of swelling pressure on temperature. In order to evaluate the predictive capabilities of the constitutive model and to increase confidence in the analysis, all its material parameters have been established on the basis of laboratory testing. The remaining input parameters for the THM formulation have been derived from previous studies.

In addition to the independent calibration based on well-controlled laboratory tests, the good agreement between field-scale modelling results and the monitored data, including cooling and partial dismantling stages, supports the use of the constitutive model for analysing the THM response of bentonite. The

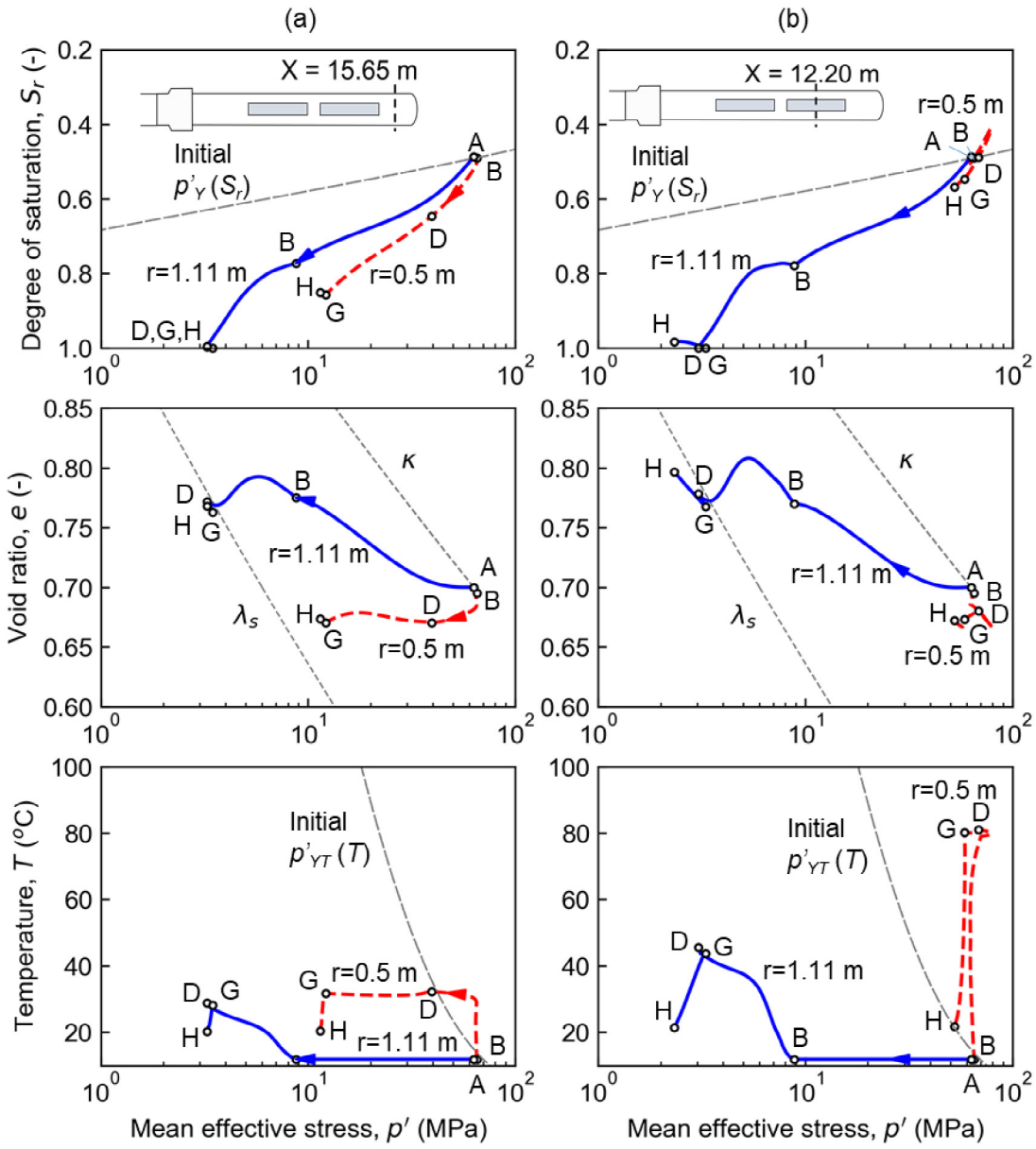

Fig. 16. Stress paths in the generalised constitutive stress space (p', S_r, e, T). (a) Section x = 15.65 (cold section) for a radial distance of r = 0.5 m and r = 1.11 m. (b) Section x = 12.20 (hot section) for a radial distance of r = 0.5 m and r = 1.11 m. The capital letters indicate a change between phases as described in the text.

model provided an insight of the causes for the final heterogeneous dry density distribution, as well as the small variations of dry density profiles between the first and second post-mortem analyses of the test. The analysis of the generalised stress paths reveals that the density gradient could be induced at the very beginning of the test operation, as a result of the strong gradients of temperature and relative humidity, that induce significant plastic strains. The dry density had a slight tendency to compensate as the hydration front progressed towards the inner parts of the EBS. However, irreversible strains that developed in the outer part of the EBS prevented the bentonite to recover the initial state, leading to permanent dry density gradients.

CRediT authorship contribution statement

Jose A. Bosch: Investigation, Formal analysis, Writing – original draft. **Yafei Qiao:** Investigation, Writing – review & editing. **Alessio Ferrari:** Supervision, Writing – review & editing. **Lyesse Laloui:** Supervision, Writing – review & editing.

Declaration of competing interest

The authors declare that they have no known competing financial interests or personal relationships that could have appeared to influence the work reported in this paper.

Data availability

Data will be made available on reasonable request

Acknowledgements

This work has received funding from the Euratom research and training programme 2014-2018 under grant agreement No 745942. The authors also thank the research group of Prof. R. Charlier and Prof. F. Collin at the University of Liège for their software LAGAMINE and advice with the implementation of the constitutive model.

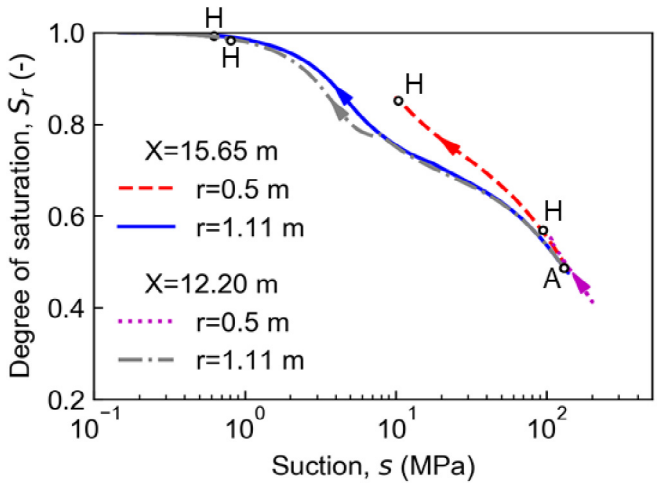

Fig. 17. Water retention behaviour of the bentonite simulated by the model at four points, located in a cold section (x = 15.65 m), and a hot section (x = 12.20 m) at radial distances of r = 0.5 m and r = 1.11 m. A indicates the common initial state and H the final state of each point.

References

1. Huertas F, Farina P, J. Farias, et al. *Full-Scale Engineered Barrier Experiment: Updated Final Report*. Technical Publication 05-0/2006; Madrid: ENRESA; 2006.
2. Gens A, Garcia-Molina AJ, Olivella S, Alonso EE, Huertas F. Analysis of a full scale in situ test simulating repository conditions. *Int J Numer Anal Methods Geomech*. 1998;22(7):515–548.
3. Alonso EE, Gens A, Josa A. A constitutive model for partially saturated soils. *Géotechnique*. 1990;40(3):405–430.
4. Lloret A, Villar MV, Sánchez M, Gens A, Pintado X, Alonso EE. Mechanical behaviour of heavily compacted bentonite under high suction changes. *Géotechnique*. 2003;53(1):27–40.
5. Gens A, Alcoverro J, Blaheta R, et al. HM and THM interactions in bentonite engineered barriers for nuclear waste disposal. *Int J Rock Mech Min Sci*. 2021;137:104572.
6. Gens A, Sánchez M, Guimarães LDN, et al. A full-scale in situ heating test for high-level nuclear waste disposal: observations, analysis and interpretation. *Geotechnique*. 2009;59(4):377–399.
7. Olivella S, Carrera J, Gens A, Alonso EE. Nonisothermal multiphase flow of brine and gas through saline media. *Transp Porous Media*. 1994;15(3):271–293.
8. Sánchez M, Gens A, Guimarães L. Thermal–hydraulic–mechanical (THM) behaviour of a large-scale in situ heating experiment during cooling and dismantling. *Can Geotech J*. 2012;49(10):1169–1195.
9. Sánchez M, Pomaro B, Gens A. Coupled THM analysis of a full-scale test for high-level nuclear waste and spent fuel disposal under actual repository conditions during 18 years of operation. *Géotechnique*. 2023:1–21.
10. Dupray F, Francois B, Laloui L. Analysis of the FEBEX multi-barrier system including thermoplasticity of unsaturated bentonite. *Int J Numer Anal Methods Geomech*. 2013;37:399–422.
11. François B, Laloui L. ACMEG-TS: A constitutive model for unsaturated soils under non-isothermal conditions. *Int J Numer Anal Methods Geomech*. 2008;32(16):1955–1988.
12. Mašín D. Coupled thermohydromechanical double-structure model for expansive soils. *J Eng Mech*. 2017;143(9):04017067.
13. Qiao Y, Xiao Y, Laloui L, Ding W, He M. A double-structure hydromechanical constitutive model for compacted bentonite. *Comput Geotech*. 2019;115:103173.
14. Wang Y, Ye WM, Wang Q, Chen YG, Cui YJ. A critical saturated state-based constitutive model for volumetric behavior of compacted bentonite. *Can Geotech J*. 2022;59(11):1872–1886.
15. Navarro V, Cabrera V, De la Morena G, Asensio L, Yustres Á, Torres-Serra J. A new double-porosity macroscopic model of bentonite free swelling. *Eng Geol*. 2022;305:106725.
16. Dieudonne AC, Della Vecchia G, Charlier R. Water retention model for compacted bentonites. *Can Geotech J*. 2017;54(7):915–925.
17. Qiao Y, Tuttolomondo A, Lu X, Laloui L, Ding W. A generalized water retention model with soil fabric evolution. *Geomech Energy Environ*. 2021;25:100205.
18. Bosch JA, Ferrari A, Laloui L. Coupled hydro-mechanical analysis of compacted bentonite behaviour during hydration. *Comput Geotech*. 2021;140:104447.
19. Bosch JA, Ferrari A, Leupin O, Laloui L. Modelling the density homogenisation of a block and granular bentonite buffer upon non-isothermal saturation. *Int J Numer Anal Methods Geomech*. 2023 1–24. http://dx.doi.org/10.1002/nag.3547.
20. Collin F, Li XL, Radu JP, Charlier R. Thermo-hydro-mechanical coupling in clay barriers. *Eng Geol*. 2002;64:179–193.
21. Collin F, Chambon R, Charlier R. A finite element method for poro mechanical modelling of geotechnical problems using local second gradient models. *Internat J Numer Methods Engrg*. 2006;65(11):1749–1772.
22. Collin F. *Couplages thermo-hydro-mécaniques dans les sols et les roches tendres partiellement saturés* [Ph.D. thesis]. Liège: Université de Liège in Department ArGEnCo; 2003.
23. Charlier R. *Approche unifiée de quelques problèmes non linéaires de mécanique des milieux continus par la méthode des éléments finis* [Ph.D. thesis]. Belgium: University of Liège; 1987.
24. Panday S, Corapcioglu MY. Reservoir transport equations by compositional approach. *Transp Porous Media*. 1989;4(4):369–393.
25. Ewen J, Thomas HR. Heating unsaturated medium sand. *Geotechnique*. 1989;39(3):455–470.
26. Philip JR, De Vries DD. Moisture movement in porous materials under temperature gradients. *EOS Trans Am Geophys Union*. 1957;38(2):222–232.
27. Nuth M, Laloui L. Effective stress concept in unsaturated soils: Clarification and validation of a unified framework. *Int J Numer Anal Methods Geomech*. 2008;32(7):771–801.
28. Laloui L, Francois B. ACMEG-t: Soil thermoplasticity model. *J Eng Mech*. 2009;135(9):932–944.
29. Collins IF, Kelly PA. A thermomechanical analysis of a family of soil models. *Geotechnique*. 2002;52(7):507–518.
30. Van Eekelen HAM. Isotropic yield surfaces in three dimensions for use in soil mechanics. *Int J Numer Anal Methods Geomech*. 1980;4(1):89–101.
31. Vilarrasa V, Parisio F, Laloui L. Strength evolution of geomaterials in the octahedral plane under nonisothermal and unsaturated conditions. *Int J Geomech*. 2017;17(7):04016152.
32. Zhou AN, Sheng D, Sloan SW, Gens A. Interpretation of unsaturated soil behaviour in the stress–saturation space, I: volume change and water retention behaviour. *Comput Geotech*. 2012;43:178–187.
33. Laloui L, Cekerevac C. Thermo-plasticity of clays: an isotropic yield mechanism. *Comput Geotech*. 2003;30(8):649–660.
34. Revil A, Lu N. Unified water isotherms for clayey porous materials. *Water Resour Res*. 2013;49(9):5685–5699.
35. Sloan SW. Substepping schemes for the numerical integration of elastoplastic stress–strain relations. *Internat J Numer Methods Engrg*. 1987;24(5):893–911.
36. Sheng D, Sloan SW, Gens A, Smith DW. Finite element formulation and algorithms for unsaturated soils. Part I: Theory. *Int J Numer Anal Methods Geomech*. 2003;27(9):745–765.
37. Romero E, Vaunat J. Retention curves of deformable clays. In: *Experimental Evidence and Theoretical Approaches in Unsaturated Soils*. CRC Press; 2000:99–114.
38. Sposito G, Prost R. Structure of water adsorbed on smectites. *Chem Rev*. 1982;82(6):553–573.
39. Jacinto AC, Villar MV, Ledesma A. Influence of water density on the water-retention curve of expansive clays. *Géotechnique*. 2012;62(8):657.
40. Villar MV, Lloret A. Influence of temperature on the hydro-mechanical behaviour of a compacted bentonite. *Appl Clay Sci*. 2004;26(1–4):337–350.
41. Villar MV. *Thermo-Hydro-Mechanical Characterisation of a Bentonite from Cabo de Gata: A Study Applied to the Use of Bentonite as Sealing Material in High-Level Radioactive Waste Repositories*. Technical Publication 01/2002; Madrid: Enresa; 2002.
42. Enresa. *Febex Project: Full-Scale Engineered Barriers Experiment for a Deep Geological Repository for High Level Radioactive Waste in Crystalline Host Rock*. Publicación técnica 1/2000; ENRESA; 2000.
43. Wang Q, Tang AM, Cui YJ, Delage P, Barnichon JD, Ye WM. The effects of technological voids on the hydro-mechanical behaviour of compacted bentonite–sand mixture. *Soils Found*. 2013;53(2):232–245.
44. A. Gens. Soil-environment interactions in geotechnical engineering. *Géotechnique*. 2010;60(1):3.
45. Pintado X, Ledesma A, Lloret A. Backanalysis of thermohydraulic bentonite properties from laboratory tests. *Eng Geol*. 2002;64(2–3):91–115.
46. Fuentes-Cantillana JL, García-Siñeriz JL, Obis J, Pérez A, Alberdi J, Barcala JM, et al. *FEBEX Full-Scale Engineered Barriers Experiment in Crystalline Host Rock, vol. 1*. Pre-Operational Stage Summary Report; ENRESA Publicación Técnica; 1998.
47. Alonso EE, et al. The FEBEX benchmark test: case definition and comparison of modelling approaches. *Int J Rock Mech Min Sci*. 2005;42(5–6):611–638.
48. Villar MV, Iglesias RJ, Garcia-Sineriz JL. State of the in situ Febex test (GTS, Switzerland) after 18 years: a heterogeneous bentonite barrier. *Environ Geotech*. 2018. http://dx.doi.org/10.1680/jenge.17.00093.
49. Ferrari A, Bosch JA, Baryla P, Rosone M. Volume change response and fabric evolution of granular MX80 bentonite along different hydro-mechanical stress paths. *Acta Geotech*. 2022;17(9):3719–3730.